



Cite this: *Chem. Commun.*, 2021, 57, 5075

Received 10th February 2021,
Accepted 14th April 2021

DOI: 10.1039/d1cc00774b

rsc.li/chemcomm

Asymmetrically strained hcp rhodium sublattice stabilized by 1D covalent boron chains as an efficient electrocatalyst†

Zhenyu Li,^{‡,ab} Xuan Ai,^{‡,ab} Hui Chen,^{‡,a} Xiao Liang,^a Xiaotian Li,^{‡,b} Dong Wang^c and Xiaoxin Zou^{‡,a}

Intermetallic rhodium boride (RhB) comprising an asymmetrically strained hcp Rh sublattice is synthesized. The covalent interaction of interstitial boron atoms is found to be the main contributor to the generation of asymmetric strains and the stabilization of the hcp Rh sublattice. In addition, RhB is identified as a hydrogen-evolving electrocatalyst with Pt-like activity, because the Rh(d)–B(s,p) orbital hybridization induces an optimized electronic structure.

Noble metals commonly form close-packed crystal structures. Some metal atoms (e.g., Ru and Os) prefer the hexagonal close-packed (hcp) structure, and the others (e.g., Rh, Ir, Pd, Pt, Ag and Au) form the cubic close-packed (ccp, also known as face-centered cubic or fcc) structure. Recently, many research attempts have been made to stabilize new metallic lattices other than the aforementioned conventional ones, and the vast majority of successful cases include the realization of fcc-metals in hcp atomic packing or *vice versa*.^{1,2} The formation of unconventional metallic lattices are mostly accessed by making changes in the environment of noble metal crystallites' growth. Suitable environmental modulators, such as growth templates, surface ligands, structural defects and interstitial atoms, have been confirmed in some cases.^{3,4} In other cases, e-beam irradiation and external pressure also can cause metallic lattice transition from the conventional to unconventional structure.^{5,6} Despite recent significant successes, the stabilization of unconventional metallic lattices is still a trial-and-error process. More efforts are required to provide a fundamental understanding of unconventional metallic lattices and crystallochemistry of noble

metals, and to explore their atomic configuration-dependent properties and functionalities.

Herein, we report the synthesis of phase-pure intermetallic rhodium boride (RhB) comprising an asymmetrically strained hcp-Rh sublattice, in which the interstitial boron atoms are covalently bonded in a single chain and different chains without direct bonding interaction are aligned parallel to the *c* axis. We find that the covalent interaction of interstitial boron atoms plays the most vital role in the stabilization of the hcp Rh sublattice, compared to other factors such as unit cell expansion, asymmetric strains and Rh–B interatomic interaction. We also show that RhB is a highly active electrocatalyst for the hydrogen evolution reaction (HER) due to its optimized electronic structure mainly governed by Rh–B interatomic orbital hybridization. Despite recent reports on the catalytic properties of some transition metal borides, RhB has never been investigated experimentally to catalyze any reactions previously.^{7–11}

We synthesized intermetallic RhB by a solid state reaction between K_3RhCl_6 and MgB_2 (details are provided in the Experimental section, ESI†). For the comparative purpose, we also synthesized metallic Rh and B-doped Rh with disordered interstitial boron distribution (dubbed B–Rh) as reference samples (Fig. S1 and S2, ESI†). The powder X-ray diffraction (XRD) patterns in Fig. 1a show that both metallic Rh and B–Rh possess the fcc structure. Despite the similarity, the diffraction peaks of B–Rh slightly shift toward the small angle side compared to those of metallic Rh, suggesting that B atoms are interstitially incorporated in the fcc-Rh lattice for B–Rh and expand the lattice volume. Unlike B–Rh, the diffraction peaks of RhB are completely different from those of metallic Rh, due to the interstitial boron ordering and hcp-Rh sublattice. The XRD pattern of RhB measured experimentally is highly consistent with the fitting plot (Fig. S3a and Table S1, ESI†), indicating the high purity of intermetallic RhB. Energy-dispersive X-ray spectroscopy (EDS) exhibits that the Rh : B atomic ratio in both RhB and B–Rh is about 1 : 1, revealing that the interstitial boron ordering in Rh–B alloy is necessary for the generation of the

^a State Key Laboratory of Inorganic Synthesis and Preparative Chemistry, College of Chemistry, Jilin University, Changchun 130012, China. E-mail: xxzou@jlu.edu.cn

^b College of Materials Science and Engineering, Jilin University, Changchun 130022, China

^c College of Chemical Engineering, Sichuan University, Chengdu 610065, China

† Electronic supplementary information (ESI) available. See DOI: 10.1039/d1cc00774b

‡ These authors contributed equally to this work.

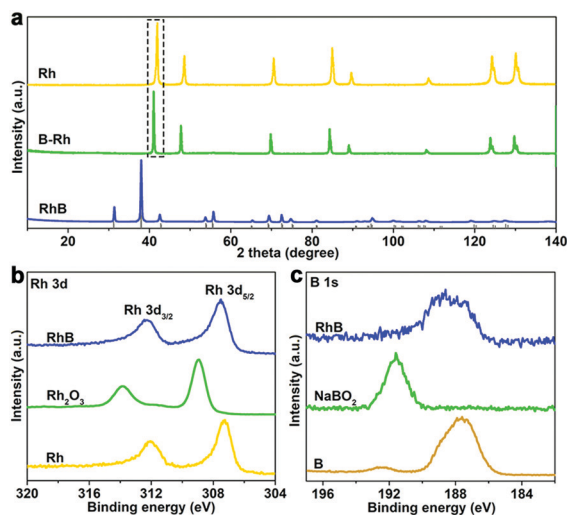


Fig. 1 (a) XRD patterns of Rh, B-Rh and RhB, using the standard cards of RhB (JCPDS 13-0289) as reference. (b) Rh 3d XPS spectra of the Rh, Rh₂O₃ and RhB. (c) B 1s XPS spectra of B, NaBO₂ and RhB.

hcp-Rh sublattice. In addition, another intermetallic rhodium boride with a lower boron content (Rh₇B₃) was also synthesized (Fig. S4–S6 and Table S2, ESI†). The Rh atoms in Rh₇B₃ form a close-packed structure, neither a fcc nor a hcp structure. This result suggests that besides interstitial ordering, a suitable amount of interstitial boron atoms is also critical for the realization of the hcp-Rh sublattice.

The scanning electron microscopy (SEM) image shows that the RhB sample is composed of particles that are 100–700 nm in size (Fig. S3b, ESI†). Further analysis using elemental mapping images (Fig. S3c, ESI†) confirms the uniform distribution of Rh and B elements over the entire particles. In the transmission electron microscopy (TEM) image (Fig. S3d, ESI†), the lattice spacing of 0.28 nm can be ascribed to the (100) crystallographic planes of RhB. The surface elemental composition and chemistry of RhB were analyzed using X-ray photoelectron spectroscopy (XPS). Fig. 1b displays Rh 3d XPS spectra of RhB and the reference samples (Rh and Rh₂O₃), and Fig. 1c shows the B 1s XPS spectra of RhB and the reference samples (B and NaBO₂). The Rh 3d and B 1s peaks of RhB do not shift in binding energy compared to those of elemental Rh and B, suggesting a negligible charge transfer between Rh and B atoms in RhB. The XPS results also suggest that an obvious surface oxide layer of RhB does not exist, again confirming the high-purity of the obtained RhB.

RhB possesses *P6₃/mmc* symmetry and a hcp-Rh sublattice, in which boron atoms occupy all of the octahedral interstices and form 1D covalent boron chains along the *c* axis (Fig. 2a). The electron location function (ELF) value between two adjacent boron atoms along the *c* axis is *ca.* 0.6, suggesting the covalent characteristic of the B–B bond (Fig. 2b). And the ELF values in a range of 0.4 to 0.5 for Rh–Rh and Rh–B bonds demonstrate that both Rh–Rh and Rh–B bonds are metallic. The strong orbital hybridization in the Rh–B and B–B pairs can also be reflected by crystal orbital Hamiltonian population

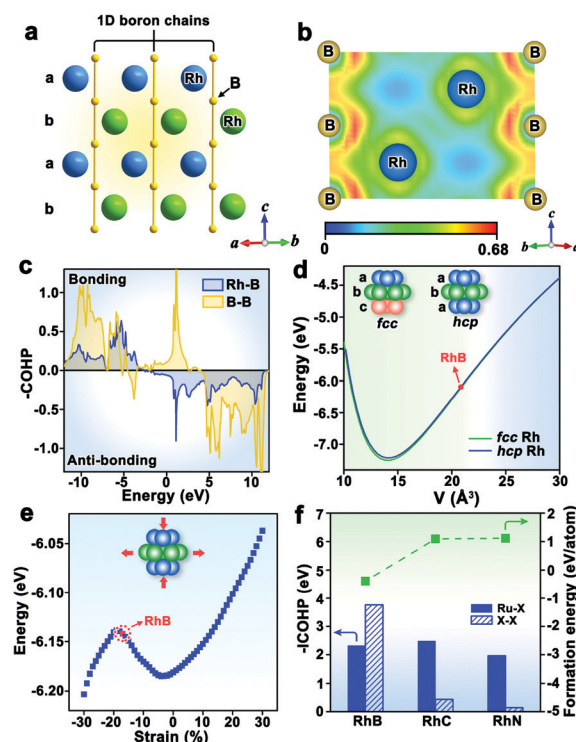


Fig. 2 (a) Crystal structure of RhB. In order to clarify the stacking pattern of the Rh sublattice, the Rh atoms are represented using blue and green spheres on the basis of the difference in their position. (b) ELF of the (110) crystallographic plane for RhB. (c) COHP curves for Ru–B and B–B pairs in RhB. (d) Equations of state for fcc-Rh and hcp-Rh lattices. Inset in (d) shows the fcc and hcp atomic arrangements of the Rh lattice. The fcc structure is an a–b–c... stacking pattern, and the hcp structure is an a–b... stacking pattern. (e) The total energy as a function of strain exerted on the hcp-Rh lattice along the *c* axis at a fixed cell volume of RhB (20.44 Å³). The inset shows a strained hcp-Rh lattice model. (f) The formation energies of RhB, RhC and RhN; and the negative integrated COHP (–ICOHP) values of Rh–X, X–X (X = B, C and N) in the three models.

(COHP) curves (Fig. 2c). The results show that there are significant contributions of bonding states below the Fermi energy for Rh–B and B–B bonds, and the bonding strength of Rh–B is weaker than that of B–B.

It is worth emphasizing that the cell volume of the hcp-Rh sublattice (20.44 Å³) of RhB is obviously larger than the optimized unit cell volume for hcp-Rh (14.11 Å³), and the *a* and *b* lattice constants of the former are greater (2.73 Å vs. 3.37 Å), with the *c* lattice constant of the former being smaller (4.37 Å vs. 4.14 Å). In other words, huge asymmetric lattice strains are exerted on the hcp-Rh sublattice of RhB: 24% tensile strain along the *a* and *b* axes, and 5% compressive strain along the *c* axis (see method for strain calculation and Table S3 and S4, ESI†). The direction of B–B bonding interaction is consistent with that of compressive strain, implying that the B–B covalent bond is possibly the origin of asymmetrically strains.

In order to better understand why the metallic sublattice of RhB is the unconventional hcp-Rh, we considered three possible factors: lattice expansion, asymmetric strains and boron-relevant electronic effect. We first compared the equations of state for fcc-Rh and hcp-Rh (Fig. 2d and Fig. S7 in ESI†), which

show their total energies as a function of unit cell volume. The result demonstrates that in a wide volume range, fcc-Rh always has a lower total energy than hcp-Rh, suggesting the higher thermodynamic stability of fcc-Rh, regardless of the expansion or compression in the cell volume. Hence, the lattice expansion is not the main reason for the stabilization of the hcp-Rh sublattice in RhB.

We also explored the effect of strain on the thermodynamic stability of the hcp-Rh lattice with a fixed unit cell volume of RhB. The total energy of the hcp-Rh lattice as a function of strain along the *c* axis is presented in Fig. 2e. The result shows that hcp-Rh can become more stable than fcc-Rh only when the compressive strain along the *c* axis is larger than 28%. But the compressive strain (17%) produced by interstitial boron atoms does not reach this critical point. Thus, the strain is also not the critical reason behind the formation of the hcp-Rh sublattice in RhB.

In order to investigate the boron-relevant electronic effect, we theoretically constructed two control structural models (*i.e.*, RhC and RhN) by replacing interstitial boron atoms of RhB with C and N atoms, respectively, and then compared their crystal and electronic structures with those of RhB. The ELF and COHP results of RhC and RhN are shown in Fig. S8 and S9 (ESI[†]), respectively. A comparison of the negative integrated Crystal Orbital Hamilton Population values (−ICOHP, a quantitative description of bonding strength) and formation energies for RhB, RhC and RhN (Fig. 2f and Table S5, ESI[†]) produces three important results. (i) Only RhB is thermodynamically stable (reflected by its negative formation energy), while RhC and RhN are thermodynamically unfavorable. Moreover, the phononic dispersion curves also show that only RhB is dynamically stable, because there is no imaginary frequency in phonon dispersion for RhB (Fig. S10, ESI[†]). (ii) The bonding strengths between Rh and B/C/N in three models are all great, with Rh–C having the strongest bonding strength. This result, together with the result (i), shows that the electronic interaction between Rh lattice and interstitial atoms is not the key cause for the stabilization of the hcp-Rh lattice. (iii) It is unique that there is a strong B–B bonding in RhB, compared with the extremely weak C–C and N–N interactions in RhC and RhN, respectively (Fig. 2f). Additionally, there is an asymmetrical strain for only RhB (Table S4, ESI[†]). These results overall demonstrate that the strong B–B covalent interaction is the main contributor to the generation of asymmetrically strains and the stabilization of the hcp-Rh sublattice in RhB.

The electrocatalytic properties of RhB toward HER in acidic electrolyte were investigated (see the Experimental section and Fig. S11 in the ESI[†]). For comparison, metallic Pt particles were also studied (Fig. S12, ESI[†]). The electrocatalytic activities of RhB, metallic Pt, metallic Rh and B–Rh were evaluated under the same conditions. Fig. 3a shows the polarization curves of RhB, Rh, B–Rh and Pt toward HER. As expected, Rh has a moderate catalytic activity, and Pt has a remarkable catalytic activity. Pt requires an overpotential of 20 mV at 10 mA cm^{−2} current density (normalized by the geometric area of the electrode). In addition, RhB and B–Rh exhibit higher catalytic

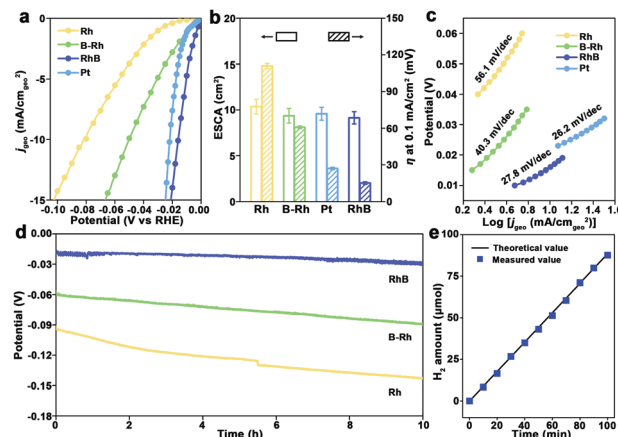


Fig. 3 (a) Linear sweep voltammetry (LSV) curves toward HER of RhB, Rh, B–Rh, and Pt in acidic solution with 85% iR-compensation. (b) Comparison of ECSAs and overpotentials at 0.1 mA cm^{−2} current density (normalized by ECSAs). (c) Tafel slopes toward HER of RhB, Rh, B–Rh, and Pt. (d) Chronopotentiometric curves of B–Rh, Rh, and B–Rh as catalysts at 10 mA cm^{−2} current density. (e) Faraday efficiency of hydrogen production over RhB at a current density of 20 mA cm^{−2} in 0.5 M H₂SO₄ solution.

activity than metallic Rh. Particularly, the overpotential required by RhB (15 mV) is even slightly lower than that required by the Pt catalyst to achieve 10 mA cm^{−2} current density. The intrinsic activities of RhB, Rh, B–Rh, and Pt are further compared by normalizing their HER currents with the corresponding electrochemical active surface area (j_{ECSA}). As shown in Fig. 3b, their intrinsic activities for HER follow the same trend as their apparent activities.

The Tafel slopes for HER of RhB, Rh, B–Rh, and Pt are also compared (Fig. 3c). Tafel slope of RhB is 27.8 mV dec^{−1}, which is comparable to that of Pt (26.2 mV dec^{−1}) and much smaller than those of Rh and B–Rh. This result demonstrates the rapid HER catalytic kinetics for RhB during the reaction process.^{12–15} The Tafel slope of ≈ 30 mV dec^{−1} also suggests that the hydrogen evolution on the RhB surface proceeds *via* a Volmer–Tafel mechanism, in which the recombination of the two adsorbed hydrogen atoms (*i.e.*, Tafel step, $\text{H}^* + \text{H}^* \rightarrow \text{H}_2$) is the rate-determining step.^{16–18}

In addition to high catalytic activity, RhB exhibits good catalytic and structural stabilities during electrocatalysis. As shown in Fig. 3d, while the catalytic activities of Rh and B–Rh decrease slowly, RhB can stably electrocatalyze HER for at least 10 h, demonstrating its high catalytic stability. The structure of RhB after a 10 h-long HER electrocatalysis was characterized. Its XRD pattern and HRTEM image show that RhB maintains its original structure after HER (Fig. S13 and S14, ESI[†]). A comparison of RhB with some representative Rh-based electrocatalysts reveals that RhB is among the most efficient Rh-based catalysts for HER both in terms of activity and stability (Table S6, ESI[†]). During the electrocatalysis, the hydrogen evolution rate of RhB is in good agreement with the theoretical value (Fig. 3e), indicating a complete electricity-to-hydrogen conversion.

In order to get better insights into the good HER catalytic activity of RhB, we calculated the hydrogen adsorption free

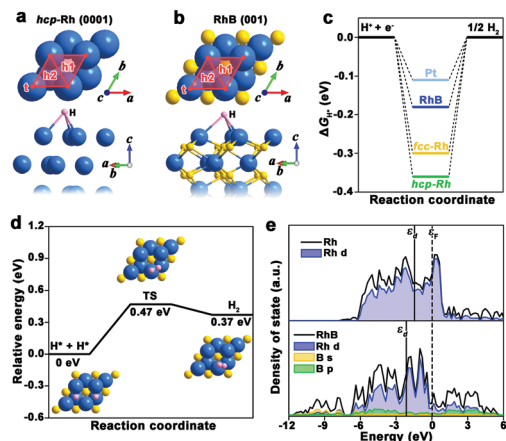


Fig. 4 Structural models for the stable hydrogen adsorption sites on (a) hcp-Rh(0001) and (b) RhB(001) surfaces. (c) The calculated free-energy diagrams at equilibrium potential for RhB(001), hcp-Rh(0001), fcc-Rh(111) and Pt(111) surfaces at a 100% H* coverage. (d) The reaction pathway for Tafel step on the RhB(001) surface. (e) Density of states (DOS) of hcp-Rh(0001) and RhB(001) surfaces. The vertical dotted line denotes the position of the Fermi energy, and the solid lines indicate the position of d-band centers.

energy (ΔG_{H^*} , a theoretical descriptor of HER activity) of close-packed surfaces for RhB and hcp-Rh. For comparison, fcc-Rh and Pt were also studied (the details of the modeling method are shown in the ESI†). The structural models for the H adsorption sites on RhB(001) and hcp-Rh(0001) surfaces are shown in Fig. 4a and b and the structural models for the H adsorption sites on fcc-Rh(111) and Pt(111) surfaces are presented in Fig. S15, ESI†. The results show that the most stable H adsorption sites of all model surfaces are the Rh₃-hollow sites (Table S7, ESI†). The calculations (Fig. 4c) reveal that RhB exhibits a smaller absolute ΔG_{H^*} value (0.18 eV) than fcc-Rh (0.30 eV) and hcp-Rh (0.36 eV), and RhB exhibits a slightly stronger hydrogen adsorption ability than Pt ($\Delta G_{H^*} = -0.11$ eV). The calculated activation energy for HER on the RhB(001) surface on the basis of the Volmer–Tafel mechanism is 0.47 eV (Fig. 4d), which is lower than that on the Pt(111) surface (0.85 eV).¹⁶ These theoretical results confirm the experimental observation on the good activity of RhB. Additionally, these theoretical results also suggest that the hcp-Rh sublattice itself does not rationalize RhB's good catalytic activity.

We next investigated the Rh–B interatomic orbital interaction on surface electronic structure and surface hydrogen adsorption properties. We calculated the density of states (DOS) of RhB(001) and hcp-Rh(0001). As revealed in Fig. 4e, there is a DOS overlap between Rh-4d band and B-2sp band, indicating the orbital hybridization between the Rh and B atoms. This is in agreement with the COHP result (Fig. S16, ESI†). Moreover, the d-band width (2.70 eV) of RhB is larger than that (2.37 eV) of hcp-Rh (Table S8, ESI†). And the d-band center of RhB (−2.12 eV) downshifts away from the Fermi level compared with that of hcp-Rh (−1.83 eV). According to the d-band theory, the lower the energy of the d-band relative to the Fermi level, the lower the energy of the antibonding states.¹⁹ As a result, the

antibonding states become more occupied and the adsorption strength of hydrogen is weakened. This explains why RhB is able to possess a Pt-like catalytic activity for HER.

In conclusion, the synthesis and structural characterization of phase-pure intermetallic rhodium boride comprising an asymmetrically strained hcp-Rh sublattice have been presented. The strong B–B covalent interreaction is responsible for the stabilization of the unconventional hcp Rh sublattice of RhB. RhB is found to be a highly efficient electrocatalyst for HER owing to its optimized surface electronic structure mainly governed by the Rh–B interatomic orbital hybridization. The results reported herein further our understanding of metallic lattices and boride-based catalysts.

X. Z. and H. C. thank the financial supports from the National Natural Science Foundation of China (NSFC) Grant No. 21922507, 21771079 and 21901083 and Fok Ying Tung Education Foundation, Grant No. 161011. The authors also thank the Fundamental Research Funds for the Central Universities, NSFC (21621001) and the 111 Project (B17020) for the additional financial support.

Conflicts of interest

There are no conflicts to declare.

Notes and references

- 1 Y. Chen, Z. Lai, X. Zhang, Z. Fan, Q. He, C. Tan and H. Zhang, *Nat. Rev. Chem.*, 2020, **4**, 243–256.
- 2 C. Sow, S. P. G. Mettela and G. U. Kulkarni, *Annu. Rev. Mater. Res.*, 2020, **50**, 345–370.
- 3 Z. Fan, Y. Chen, Y. Zhu, J. Wang, B. Li, Y. Zong, Y. Han and H. Zhang, *Chem. Sci.*, 2017, **8**, 795–799.
- 4 H. Chen, X. Ai, W. Liu, Z. Xie, W. Feng, W. Chen and X. Zou, *Angew. Chem., Int. Ed.*, 2019, **58**, 11409–11413.
- 5 Q. Li, W. Niu, X. Liu, Y. Chen, X. Wu, X. Wen, Z. Wang, H. Zhang and Z. Quan, *J. Am. Chem. Soc.*, 2018, **140**, 15783–15790.
- 6 J. Li, J. Chen, H. Wang, N. Chen, Z. Wang, L. Guo and F. L. Deepak, *Adv. Sci.*, 2018, **5**, 1700992.
- 7 Y. Chen, G. Yu, W. Chen, Y. Liu, G. Li, P. Zhu, Q. Tao, Q. Li, J. Liu, X. Shen, H. Li, X. Huang, D. Wang, T. Asefa and X. Zou, *J. Am. Chem. Soc.*, 2017, **139**, 12370–12373.
- 8 X. Ai, X. Zou, H. Chen, Y. Su, X. Feng, Q. Li, Y. Liu, Y. Zhang and X. Zou, *Angew. Chem., Int. Ed.*, 2020, **59**, 3961–3965.
- 9 X. Zou, L. Wang, X. Ai, H. Chen and X. Zou, *Chem. Commun.*, 2020, **56**, 3061–3064.
- 10 Q. Li, L. Wang, X. Ai, H. Chen, J. Zou, G. Li and X. Zou, *Chem. Commun.*, 2020, **56**, 13983–13986.
- 11 E. Lee, H. Park, H. Joo and B. P. T. Fokwa, *Angew. Chem., Int. Ed.*, 2020, **59**, 11774–11778.
- 12 X. Hu, Y. Yin, W. Liu, X. Zhang and H. Zhang, *Chin. J. Catal.*, 2019, **40**, 1085–1092.
- 13 Y. Zhu, Q. Lin, Y. Zhong, H. A. Tahini, Z. Shao and H. Wang, *Energy Environ. Sci.*, 2020, **13**, 3361–3392.
- 14 Y. Zhu, H. A. Tahini, Z. Hu, J. Dai, Y. Chen, H. Sun, W. Zhou, M. Liu, S. C. Smith, H. Wang and Z. Shao, *Nat. Commun.*, 2019, **10**, 149.
- 15 H. Chen, X. Liang, Y. Liu, X. Ai, T. Asefa and X. Zou, *Adv. Mater.*, 2020, **32**, 2002435.
- 16 Q. Chen, Y. Nie, M. Ming, G. Fan, Y. Zhang and J. Hu, *Chin. J. Catal.*, 2020, **41**, 1791–1811.
- 17 P. Li and W. Chen, *Chin. J. Catal.*, 2019, **40**, 4–22.
- 18 J. Dai, Y. Zhu, H. A. Tahini, Q. Lin, Y. Chen, D. Guan, C. Zhou, Z. Hu, H. J. Lin, T. S. Chan, C. T. Chen, S. C. Smith, H. Wang, W. Zhou and Z. Shao, *Nat. Commun.*, 2020, **11**, 5657.
- 19 Q. Li, Y. Ouyang, S. Lu, X. Bai, Y. Zhang, L. Shi, C. Ling and J. Wang, *Chem. Commun.*, 2020, **56**, 9937–9949.